Thermoporoelastic AVO modeling of Olkaria geothermal reservoirs

SUBMISSION DATE / POSTED DATE

04-02-2023 / 07-02-2023

DOI

10.36227/techrxiv.22010273.v1

Thermoporoelastic AVO modeling of Olkaria geothermal reservoirs

Yifan Cheng[1,2], Li-Yun Fu[1,2,3*], Wanting Hou[1,2], José M. Carcione[4], Wubing Deng[1,2,3], Zhiwei Wang[1,2,3]

[1]Shandong Provincial Key Laboratory of Deep Oil and Gas, China University of Petroleum (East China), Qingdao 266580, China.
[2]School of Geosciences, China University of Petroleum (East China), Qingdao 266580, China.
[3]Laboratory for Marine Mineral Resources, Qingdao National Laboratory for Marine Science and Technology, Qingdao 266071, China.
[4]Nazional Institute of Oceanography and Geophysics (OGS), Trieste 34010, Italy
*Corresponding author: lfu@upc.edu.cn (Li-Yun Fu)

ABSTRACT

Seismic AVO has a significant potential for fluid identification in time-lapse monitoring of the cyclic recovery of geothermal reservoirs. With this goal, we develop an AVO method based on the reflection and transmission (R/T) of elastic waves at an interface between two fluid-saturated thermo-poroelastic media. The method is applied to the Olkaria geothermal reservoirs in Kenya. This system is characteristic of a natural cyclic recovery, where cyclic meteoric water undergoes complex phase transition and thermo-hydro-mechanical coupling process. Conceptual models are built based on petrophysical and thermophysical properties of trachyte thermal reservoirs in the eastern field, with an attempt to model the shallow steam and deep boiling water zones. A plane-wave analysis illustrates the effects of thermal conductivity, specific heat, and porosity on velocity dispersion and attenuation of the fast-P, Biot slow-P, and thermal slow-P waves. AVO modeling by P-wave incidence is conducted to investigate the effects of temperature, porosity, specific heat, and fluid type on the R/T coefficients. For trachyte reservoirs with a temperature less than 400°C, limited changes in the thermophysical properties (e.g., thermal conductivity and specific heat) have negligible effects on wave propagation, whereas significant effects are due to temperature, porosity, and fluid type. Particularly, comparisons of cyclic recovery using water, supercritical CO_2, and gas (dry case) as the heat transfer fluid, demonstrate that the crossplot of fluid factors and intercept gradient (PG) can be used as a precursor to hydrofracturing-induced permeability, fluid leakage or short circuits.

Keywords: Geothermal reservoir, AVO response, thermo-poroelastic AVO method, wave propagation, seismic monitoring

INTRODUCTION

Geothermal fields provide a clean and low-carbon renewable energy with large storage capacity. Enhanced geothermal system (EGS), as an economic development pattern, has been widely used to extract heat by creating an artificial circulation system of fluids (e.g., water or CO_2) through fracturing techniques to enhance the porosity and permeability of hot dry rocks (Pandey et al., 2018). EGSs involve a complex thermo-hydro-mechanical coupling process (Breede et al., 2013; Olasolo et al., 2016; Lu, 2018), where geophysical properties play a crucial role. The thermo-poroelastic AVO modeling developed in this work has the potential to enable time-lapse reflection seismic monitoring for EGSs.

We consider the Olkaria geothermal system in Kenya as a natural EGS (e.g., Ofwona, 2002; West-JEC, 2009; Shi et al., 2021), where meteoric water percolates down along the major fractures and partly from infiltration. The groundwater flows laterally due to pressure difference and recharges into the geothermal system, where it is heated and then rises in the upflow zones. The upward steam condenses below the cap rock and sinks again in a kind of convective cycle.

Geophysical techniques have been widely used to investigate subsurface conditions of geothermal resources, such as temperature gradients, fracture networks, and petrophysical properties (Willis et al., 2010). Real-time (or near real-time) seismic monitoring is critical for evaluating the operational efficiency and stability of geothermal reservoirs (Berard and Cornet, 2003). Magnetotelluric inversion (Chen et al. 2012) and time-lapse monitoring (Peacock et al., 2013) were applied to EGS for analyzing the direction of fluid migration. Microearthquake and ground-noise surveys are also of interest in geothermal exploration (Lehujeur et al., 2015; Rathnaweera et al., 2020). Kent and Louie (2013) correlate azimuthal anisotropy to geothermal-resource potential using a 3D-3C seismic survey. Particularly, high-resolution 3D seismic imaging (Salaun et al., 2020) can reveal the distribution of fracture networks of a deep reservoir. Many researches show that comprehensive geophysical data can be used to describe geothermal reservoirs (e.g., Colwell et al., 2012; Patterson et al., 2017; Vasco et al., 2020) and reduce the risk of exploration (Guitton, 2020). These studies focus on the application of seismic techniques, which generally requires a proper understanding of the temperature-dependent physical properties and effects on the seismic response. Numerous experimental studies have been conducted to investigate the sensitivity of seismic properties to temperature variations (e.g., Batzle and Wang, 1992; Yang et al., 2019, 2021; Qi et al., 2021). Poletto et al. (2018) present a theory and sensitivity analysis based on the Burgers model for brittle–ductile behavior, integrated with a modified Gassmann model for fluid saturated porous rocks, pressure effects, as well as squirt-flow loss. Pressure-Temperature effects on the elastic properties of geothermal rocks are important mainly in relation to seismic-reflection technology, whose physics is relevant to the behavior of reflection and transmission (R/T) of elastic waves.

Amplitude variation with offset (AVO) (e.g., Shuey, 1985; Fawad et al., 2020) is one method used to estimate the properties of reservoirs. Conventional AVO methods cannot be directly applied to geothermal reservoirs because they do not consider temperature effects on both the rock and fluid properties. For this purpose, we use the theory of thermoelasticity to obtain the R/T coefficients of elastic waves, based on the Lord-Shulman (LS) approach (Lord and Shulman, 1967), that has been applied to investigate the effect of the thermophysical properties on wave propagation in non-porous media (Carcione et al., 2018; Wang et al., 2020; Hou et al., 2021). The theory predicts a classical P wave, a slow P diffusive wave (thermal mode), and an S wave. These two P-wave modes are similar to those of classical poroelasticity, with the difference that the slow P wave is caused by heat flow (not to fluid flow as in poroelasticity). The thermal mode is diffusive at low frequencies. The R/T phenomena of thermoelastic waves have been extensively studied. For instance, a comprehensive review (Hou et al., 2022a) identifies existing mistakes and flaws in previous studies, especially when ignoring the presence of inhomogeneous plane waves. Based on the R/T of waves incident at a preheated interface (Hou et al., 2022a) and their propagation in multilayered thermal media (Hou et al., 2022b), Hou et al. (2022c) extend the conventional AVO method to thermoelastic media for seismic exploration of superdeep high-temperature oil/gas resources.

The LS theory has been extended to the porous case (i.e., the so-called thermo-poroelasticity) by incorporating Biot poroelasticity to couple elastic deformations with temperature (Noda, 1990; Nield and Bejan, 2006; Sharma, 2008; Carcione et al., 2019;

Baldonedo et al., 2020). The theory predicts the presence of both Biot and thermal slow P waves besides the classical P and S waves. Numerical simulations by the Fourier pseudospectral method (Carcione et al., 2019) show that the conversion from fast waves to thermal modes leads to mesoscopic energy attenuation. Wei et al. (2020) develop a frequency-domain Green's function as a displacement-temperature solution of thermo-poroelasticity to investigate the effect of fluid viscosities and thermophysical properties. Based on the Biot-Rayleigh double-porosity theory (Ba et al., 2011), Li et al. (2022a) extend the LS thermo-poroelasticity to the case of double porosity by taking into account the local heat/fluid flows in two types of pores. The double-porosity thermo-poroelasticity theory has been used to develop a thermo-hydro-mechanical model (Li et al., 2022b) for the evaluation of the seismic properties of geothermal reservoirs in the cyclic recovery of fractured-vuggy geothermal reservoirs. Regarding the R/T phenomena of thermo-poroelastic waves, Wang et al. (2021) studied the reflection of inhomogeneous plane waves at a free surface. Hou et al. (2022d) further investigated the R/T of inhomogeneous plane waves at the interface between two fluid-saturated thermo-poroelastic media. In this work, we investigate thermo-poroelastic AVO, based on the thermo-poroelastic R/T coefficients.

We first introduce the theory of thermo-poroelasticity and then formulate the AVO method. We consider the Olkaria geothermal field in Kenya, based on a previous study (Fu, 2019). We conduct a plane-wave analysis to investigate the effect of the thermal properties on wave velocity and attenuation. Finally, the AVO response is investigated for the effect of temperatures, porosities and fluids. We demonstrate that the velocity dispersion and angle-dependent amplitude due to thermal effects with water or CO_2 offer an important indicator that could be potentially used to monitor the operation efficiency of EGSs.

WAVE PROPAGATION THEORY

The LS thermo-poroelasticity theory describes wave loss due to fluid and heat flows, due to the presence of the Biot and thermal slow P waves. The theory can be used to describe wave propagation in geothermal reservoirs.

Lord and Shulman (1967) generalize Biot (1956) by introducing a relaxation time τ to the classical heat-conduction equation, which can be further extended for porous media as (Nield and Bejan, 2006; Sharma, 2008; Carcione et al., 2019; Wei et al., 2020)

$$\gamma T_{,ii} = \rho c(\dot{T} + \tau\ddot{T}) + \beta T_0\left[\left(\dot{u}_{i,i} + \dot{w}_{i,i}\right) + \tau\left(\ddot{u}_{i,i} + \ddot{w}_{i,i}\right)\right], \tag{1}$$

where T is the increment of temperature over a reference T_0, γ is the thermal conductivity, c is the specific heat, $\rho = (1-\phi)\rho_s + \phi\rho_f$ is the composite density with ρ_s and ρ_f the grain and fluid densities, respectively, ϕ is the bulk porosity, u_i and w_i are the displacement components in the solid and fluid phases, respectively, the thermal modulus $\beta = \beta_s + \alpha\beta_f$, with β_s and β_f the coefficients of thermal stress for the solid and fluid phases, respectively, and a dot above a variable denotes the time differentiation,

The constitutive relations of thermo-poroelasticity for the stress components σ_{ij}, displacement components (u_i and w_i), and pore-fluid pressure p_f are (Carcione et al., 2019)

$$\begin{cases} \sigma_{ij} = \lambda\delta_{ij}u_{k,k} + \mu\left(u_{i,j} + u_{j,i}\right) + \alpha M\delta_{ij}\left(\alpha u_{k,k} + w_{k,k}\right) - \beta\delta_{ij}T \\ -\rho_f = M\left(\alpha u_{i,i} + \omega_{i,i}\right) - \frac{\beta_f}{\phi}T \end{cases}, \tag{2}$$

where λ and μ are the Lamé constants of the drained matrix, δ_{ij} is the Kronecker delta, and

$$\begin{cases} \alpha = 1 - \frac{K_m}{K_s} \\ M = \frac{K_s}{1-\phi-K_m/K_s+\phi K_s/K_f} \\ K_m = \lambda + \frac{2}{3}\mu \end{cases}, \tag{3}$$

where K_s and K_f are the solid and fluid bulk moduli, respectively.

The wave equations for the displacement components and temperature fluctuations in an isotropic porous medium saturated with a viscous fluid are (Carcione et al., 2019)

$$\begin{cases} \rho\ddot{u}_i + \rho_f\ddot{w}_i = (\lambda + \mu + \alpha^2 M)u_{j,ij} + \mu u_{i,jj} + \alpha M w_{j,ij} - \beta T_{,i} \\ \rho_f\ddot{u}_i + q\ddot{w}_i + r\dot{w}_i = M\left(\alpha u_{j,ij} + w_{j,ij}\right) - \frac{\beta_f}{\phi}T_{,i} \\ \gamma T_{,ii} = \rho c\left(\dot{T} + \tau\ddot{T}\right) + \beta T_0[\dot{u}_{i,i} + \dot{w}_{i,i} + \tau(\ddot{u}_{i,i} + \ddot{w}_{i,i})] \end{cases}, \tag{4}$$

where $r = \eta/\kappa$, with η the fluid viscosity and κ the permeability, and $q = \zeta\rho_f/\phi$, with ζ the tortuosity. It should be stressed that the thermo-strain coupling in Eq. (4) is only concerned with the bulk strain and is independent of the shear strain, that is, the shear wave (S wave) is not affected by temperature (in homogeneous media). The equation assumes that the solid and fluid phases have the same temperature.

To obtain the phase velocity and attenuation of the different wave modes, we consider the following plane-wave analysis by expressing the displacement and temperature as plane waves,

$$\begin{cases} u_i = A s_i e^{i\omega(t - \frac{l_j}{v_c} x_j)} \\ w_i = B d_i e^{i\omega(t - \frac{l_j}{v_c} x_j)}, \\ T = C e^{i\omega(t - \frac{l_j}{v_c} x_j)} \end{cases} \tag{5}$$

where A, B and C are amplitude constants, s_i and d_i are vectors, ω is the angular frequency, v_c is the complex velocity, t is the travel time, l_j denotes the propagation directions, x_j are the position components, and $i = \sqrt{-1}$.

Substituting Eq. (5) into (4) and considering P-wave propagation parallel to the direction of displacement (i.e., $s_i l_i = d_i l_i = 1$), we obtain the dispersion relation (Wei et al., 2020),

$$b_1 (v_c^2)^3 + b_2 (v_c^2)^2 + b_3 v_c^2 + b_4 = 0, \tag{6}$$

where

$$\begin{cases} b_1 = \rho c \phi N(\omega L - i r \rho) \\ b_2 = i\phi r K - \omega(r\phi(\gamma\rho + \tau K) + \phi\rho c H + T_0 \beta J) - i\omega^2(\phi(\gamma L + \rho c H \tau) + T_0 \beta J \tau) \\ b_3 = \omega(\phi(\rho c M E + r\gamma F) + T_0 \beta G) + i\omega^2(\phi(\gamma H + \rho c M E \tau) + T_0 \beta G \tau) \\ b_4 = -i\omega^2 \gamma \phi M E \end{cases}, \tag{7}$$

with

$$\begin{cases} E = \lambda + 2\mu,\ F = E + \alpha^2 M,\ G = E\beta_f + M(\alpha - 1)(\alpha\beta_f - \phi\beta) \\ H = qF + \rho M - 2\alpha M \rho_f, J = \beta_f(\rho - \rho_f) + \phi\beta(q - \rho_f), K = \rho c F + T_0 \beta^2, \\ L = q\rho - \rho_f^2, N = 1 + i\omega\tau \end{cases} \tag{8}$$

The relations describe the dispersion and attenuation characteristics of wave propagation in thermo-poroelastic media. The fast P waves are dissipative due to the coupling with the fluid and heat flow. If $\beta = \beta_f = 0$, we get a quadratic equation in v_c, which correspond to Biot velocities for the fast and slow P waves:

$$(-ib_\rho + \omega m_\rho - \omega\rho_f^2) v_c^4 + (ibE_G - \omega m E_G - \omega M_\rho + 2\omega\alpha M_{\rho f}) v_c^2 + \omega M E = 0, \tag{9}$$

and an additional root

$$v_c = \sqrt{\frac{i\omega a^2}{1 + i\omega\tau}},\ a = \sqrt{\frac{\gamma}{c}}, \tag{10}$$

where a is the thermal diffusivity (Carcione et al., 2019). The phase velocity and attenuation factor can be obtained from the complex velocity as

$$v_p = [Re(v_c^{-1})]^{-1} \ \text{and} \ A = -\omega Im(v_c^{-1}), \tag{11}$$

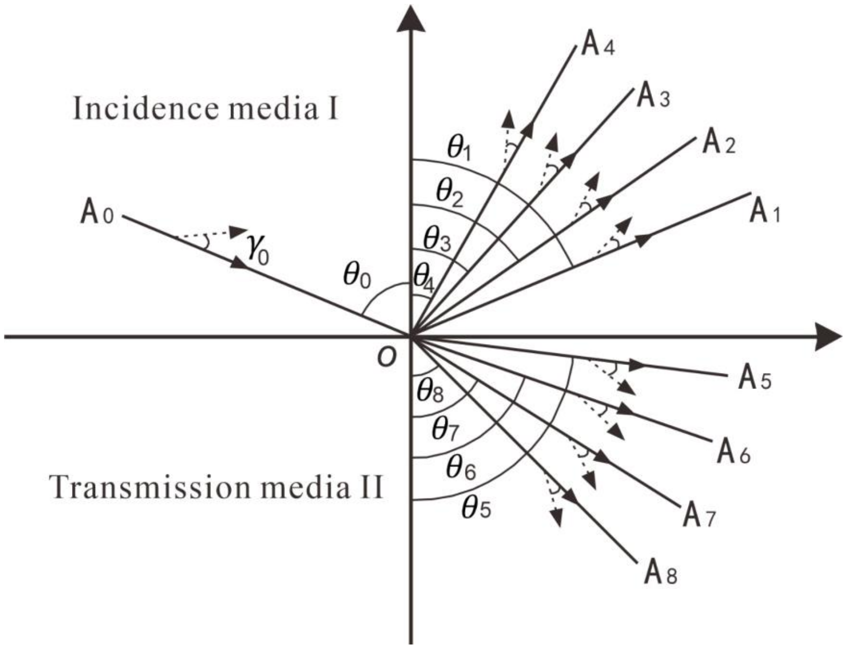

Figure 1. Scheme of the reflection and transmission of inhomogeneous plane waves at an interface between two thermo-poroelastic media, where γ_0 is the incident-wave inhomogeneity angle between the attenuation (dashed arrow) and propagation (solid arrow) directions.

THE AVO METHOD

Figure 1 shows a diagram of the reflection and transmission of an inhomogeneous plane wave incident at an interface between two thermo-poroelastic media. We use the superscripts I and II to denote the incidence (z>0) and transmission (z<0) media. The incident wave generates reflected fast P (P1), Biot slow P (P2), thermal slow P (P3), and shear (S) waves in the upper-medium I and four transmitted waves in the lower-medium II. The amplitude A_0 is related to the incident wave, while A_1, A_2, A_3, and A_4 (A_5, A_6, A_7, and A_8) to the reflected (transmitted) P1, P2, P3, and S waves, respectively. The eight boundary conditions between the two half-spaces (z=0) are (Ignaczak and Ostoja-Starzewski, 2010),

$$\begin{gathered}
u_z^{\mathrm{I}} = u_z^{\mathrm{II}},\ u_x^{\mathrm{I}} = u_x^{\mathrm{II}},\ \sigma_{zz}^{\mathrm{I}} = \sigma_{zz}^{\mathrm{II}},\ \sigma_{xz}^{\mathrm{I}} = \sigma_{xz}^{\mathrm{II}}, \\
\phi^{\mathrm{I}}(w_z^{\mathrm{I}} - u_z^{\mathrm{I}}) = Q\phi^{\mathrm{II}}(w_z^{\mathrm{II}} - u_z^{\mathrm{II}}),\ Qp^{\mathrm{I}} = Qp^{\mathrm{II}} + (1-Q)\phi^{\mathrm{II}}(w_z^{\mathrm{II}} - u_z^{\mathrm{II}}), \\
T^{\mathrm{I}} = T^{\mathrm{II}}, \kappa^{\mathrm{I}}\frac{\partial T^{\mathrm{I}}}{\partial z} = \kappa^{\mathrm{II}}\frac{\partial T^{\mathrm{II}}}{\partial z},
\end{gathered} \tag{12}$$

where Q=0 and 1 denote impermeable (pores sealed) and permeable (pores open) boundaries, respectively.

The potential functions of plane waves for the case of P-wave incidence are

$$\phi_s^l = \phi_0^s + \sum_{a=m}^{n} \phi_a^s, \quad \phi_f^l = \phi_0^f + \sum_{a=m}^{n} \phi_a^f,$$

$$\psi_s^l = \psi_b^s, \quad \psi_f^l = \psi_b^f, \tag{13}$$

where for the incidence (reflection) medium (l denotes I), m=1, n=3, and b=4, whereas for the transmission medium (l denotes II), m=5, n=7, b=8, and the coefficients of the potential functions with subscript 0 are zero. The displacement potentials are

$$\phi_a = A_a \exp[i(\omega t - \mathbf{k}_a \cdot \mathbf{x})], a = 0, 1, \ldots, 7 \text{ and } \neq 4$$

$$\psi_b = A_b \exp[i(\omega t - \mathbf{k}_b \cdot \mathbf{x})], b = 4, 8. \tag{14}$$

The wave vectors are

$$\mathbf{k}_c \cdot \mathbf{x} = p_c x + q_c z, c = 0, 1, \ldots 8, \tag{15}$$

where the horizontal wavenumber p_c remains unchanged during the propagation, following the generalized Snell law (Borcherdt, 2009) with

$$p_c = |k| \sin\theta - i|\alpha| \sin(\theta - \gamma) \ . \tag{16}$$

The vertical wavenumber q_c can be obtained from the complex wavenumbers k_c as

$$q_c = D_R + iD_I, D = \pm pv\sqrt{k_c^2 - p_c^2}, \tag{17}$$

where pv denotes the principal value. The downward waves correspond to the minus sign otherwise the positive sign holds to ensure the decay of the reflected and transmitted waves along the positive z-direction.

Substituting the constitutive relation and the potential functions into the boundary conditions, we obtain the Knott equations for the incident P wave as

$$\begin{bmatrix} a_{11} & a_{12} & a_{13} & a_{14} & a_{15} & a_{16} & a_{17} & a_{18} \\ a_{21} & a_{22} & a_{23} & a_{24} & a_{25} & a_{26} & a_{27} & a_{28} \\ a_{31} & a_{32} & a_{33} & a_{34} & a_{35} & a_{36} & a_{37} & a_{38} \\ a_{41} & a_{42} & a_{43} & a_{44} & a_{45} & a_{46} & a_{47} & a_{48} \\ a_{51} & a_{52} & a_{53} & a_{54} & a_{55} & a_{56} & a_{57} & a_{58} \\ a_{61} & a_{62} & a_{63} & a_{64} & a_{65} & a_{66} & a_{67} & a_{68} \\ a_{71} & a_{72} & a_{73} & a_{74} & a_{75} & a_{76} & a_{77} & a_{78} \\ a_{81} & a_{82} & a_{83} & a_{84} & a_{85} & a_{86} & a_{87} & a_{88} \end{bmatrix} \begin{bmatrix} A_1/A_0 \\ A_2/A_0 \\ A_3/A_0 \\ A_4/A_0 \\ A_5/A_0 \\ A_6/A_0 \\ A_7/A_0 \\ A_8/A_0 \end{bmatrix} = \begin{bmatrix} a_{19} \\ a_{29} \\ a_{39} \\ a_{49} \\ a_{59} \\ a_{69} \\ a_{79} \\ a_{89} \end{bmatrix}, \tag{18}$$

where

$$
\left\{
\begin{gathered}
a_{11} = q_1, a_{12} = q_2, a_{13} = q_3, a_{14} = p_4, \\
a_{15} = q_5, a_{16} = q_6, a_{17} = q_7, a_{18} = -p_8, \\
a_{19} = q_0, a_{21} = p_1, a_{22} = p_2, a_{23} = p_3, a_{24} = -q_4, \\
a_{25} = -p_5, a_{26} = -p_6, a_{27} = -p_7, a_{28} = -q_8, a_{29} = -p_0 \\
a_{31} = k_1^2(-M^{\mathrm{I}}(\alpha^{\mathrm{I}})^2 - M^{\mathrm{I}}\alpha^{\mathrm{I}}V_1 - \lambda^{\mathrm{I}}) + \delta_1\beta^{\mathrm{I}}(i\omega_{T1} - 1) - 2\mu^{\mathrm{I}}q_1^2, \\
a_{32} = k_2^2(-M^{\mathrm{I}}(\alpha^{\mathrm{I}})^2 - M^{\mathrm{I}}\alpha^{\mathrm{I}}V_2 - \lambda^{\mathrm{I}}) + \delta_2\beta^{\mathrm{I}}(i\omega_{T1} - 1) - 2\mu^{\mathrm{I}}q_2^2, \\
a_{33} = k_3^2(-M^{\mathrm{I}}(\alpha^{\mathrm{I}})^2 - M^{\mathrm{I}}\alpha^{\mathrm{I}}V_3 - \lambda^{\mathrm{I}}) + \delta_3\beta^{\mathrm{I}}(i\omega_{T1} - 1) - 2\mu^{\mathrm{I}}q_3^2, \\
a_{34} = -2\mu^{\mathrm{I}}p_4q_4, \\
a_{35} = k_5^2(-M^{\mathrm{II}}(\alpha^{\mathrm{II}})^2 - M^{\mathrm{II}}\alpha^{\mathrm{II}}V_5 - \lambda^{\mathrm{II}}) + \delta_5\beta^{\mathrm{II}}(i\omega_{T1} - 1) - 2\mu^{\mathrm{II}}q_5^2, \\
a_{36} = k_3^2(-M^{\mathrm{II}}(\alpha^{\mathrm{II}})^2 - M^{\mathrm{II}}\alpha^{\mathrm{II}}V_6 - \lambda^{\mathrm{II}}) + \delta_6\beta^{\mathrm{II}}(i\omega_{T1} - 1) - 2\mu^{\mathrm{II}}q_3^2, \\
a_{37} = k_3^2(-M^{\mathrm{II}}(\alpha^{\mathrm{II}})^2 - M^{\mathrm{II}}\alpha^{\mathrm{II}}V_7 - \lambda^{\mathrm{II}}) + \delta_7\beta^{\mathrm{II}}(i\omega_{T1} - 1) - 2\mu^{\mathrm{II}}q_3^2, \\
a_{38} = -2\mu^{\mathrm{II}}p_8q_8, \\
a_{39} = k_0^2(M^{\mathrm{I}}(\alpha^{\mathrm{I}})^2 + M^{\mathrm{I}}\alpha^{\mathrm{I}}V_0 + \lambda) - \delta_0\beta^{\mathrm{I}}(i\omega_{T1} - 1) + 2\mu^{\mathrm{I}}q_0^2, \\
a_{41} = 2\mu^{\mathrm{I}}p_1q_1,\ a_{42} = 2\mu^{\mathrm{I}}p_2q_2,\ a_{43} = 2\mu^{\mathrm{I}}p_3q_3,\ a_{44} = \mu^{\mathrm{I}}(p_4^2 - q_4^2), \\
a_{45} = 2\mu^{\mathrm{II}}p_5q_5,\ a_{46} = 2\mu^{\mathrm{II}}p_6q_6,\ a_{47} = 2\mu^{\mathrm{II}}p_7q_7, \\
a_{48} = -\mu^{\mathrm{II}}(p_8^2 - q_8^2),\ a_{49} = 2\mu^{\mathrm{I}}p_0q_0, \\
a_{51} = \phi^{\mathrm{I}}q_1(V_1 - 1),\ a_{52} = \phi^{\mathrm{I}}q_2(V_2 - 1),\ a_{53} = \phi^{\mathrm{I}}q_3(V_3 - 1), \\
a_{54} = \phi^{\mathrm{II}}p_4(V_4 - 1),\ a_{55} = \phi^{\mathrm{II}}q_5(V_5 - 1),\ a_{56} = \phi^{\mathrm{II}}q_5(V_5 - 1), \\
a_{57} = \phi^{\mathrm{II}}q_7(V_7 - 1),\ a_{58} = -\phi^{\mathrm{II}}p_8(V_8 - 1),\ a_{59} = \phi^{\mathrm{I}}q_0(V_0 - 1), \\
a_{61} = k_1^2M^{\mathrm{I}}(V_1 + \alpha^{\mathrm{I}}) - \frac{\delta_1\beta_f^{\mathrm{I}}}{\phi^{\mathrm{I}}}(i\omega_{T2} - 1), \\
a_{62} = k_2^2M^{\mathrm{I}}(V_2 + \alpha^{\mathrm{I}}) - \frac{\delta_2\beta_f^{\mathrm{I}}}{\phi^{\mathrm{I}}}(i\omega_{T2} - 1), \\
a_{63} = k_3^2M^{\mathrm{I}}(V_3 + \alpha^{\mathrm{I}}) - \frac{\delta_3\beta_f^{\mathrm{I}}}{\phi^{\mathrm{I}}}(i\omega_{T2} - 1), \\
a_{64} = 0,\ a_{68} = 0, \\
a_{65} = -k_5^2M^{\mathrm{II}}(V_5 + \alpha^{\mathrm{II}}) - \frac{\delta_5\beta_f^{\mathrm{II}}}{\phi^{\mathrm{II}}}(i\omega_{T21} - 1), \\
a_{66} = -k_6^2M^{\mathrm{II}}(V_6 + \alpha^{\mathrm{II}}) - \frac{\delta_6\beta_f^{\mathrm{II}}}{\phi^{\mathrm{II}}}(i\omega_{T21} - 1), \\
a_{67} = -k_7^2M^{\mathrm{II}}(V_7 + \alpha^{\mathrm{II}}) - \frac{\delta_7\beta_f^{\mathrm{II}}}{\phi^{\mathrm{II}}}(i\omega_{T21} - 1), \\
a_{69} = -k_0^2M^{\mathrm{I}}(V_0 + \alpha^{\mathrm{I}}),\ a_{71} = \delta_1,\ a_{72} = \delta_2,\ a_{73} = \delta_3, \\
a_{74} = 0,\ a_{75} = \delta_5,\ a_{76} = \delta_6,\ a_{77} = \delta_7,\ a_{78} = 0, \\
a_{79} = -\delta_0,\ a_{81} = \gamma^{\mathrm{I}}\delta_1q_1,\ a_{82} = \gamma^{\mathrm{I}}\delta_2q_2,\ a_{83} = \gamma^{\mathrm{I}}\delta_3q_3,\ a_{84} = 0, \\
a_{85} = \gamma^{\mathrm{II}}\delta_5q_5,\ a_{86} = \gamma^{\mathrm{II}}\delta_6q_6, a_{87} = \gamma^{\mathrm{II}}\delta_7q_7,\ a_{88} = 0, \\
a_{89} = \gamma^{\mathrm{I}}\delta_0q_0,
\end{gathered}
\right.
\tag{19}
$$

and

$$
V_a = \frac{\beta\bar{\phi}\bar{\tau}_1\big(M\bar{\alpha}(p_0^2 + q_0^2) - \omega^2\rho_f\big) - \bar{\tau}_2\beta_f((E + \bar{\alpha}^2M)(p_0^2 + q_0^2) - \rho\omega^2)}{\beta\bar{\phi}\bar{\tau}_1\big(m\omega^2 + ib\omega - M(p_0^2 + q_0^2)\big) + \bar{\tau}_2\beta_f(M\bar{\alpha}(p_0^2 + q_0^2) - \omega^2\rho_f)},
$$

$$
\delta_a = \frac{i\omega\beta\overline{\tau_4}T_0(1+V_a)(p_0^2+q_0^2)}{i\omega\overline{\tau_2}c - \bar{\gamma}(p_0^2+q_0^2)},\ \ a = 0, 1, \ldots, 7\ and\ \neq 4 \tag{20}
$$

$$V_b = \frac{-\omega\rho_f}{m\omega + i\eta/\bar{\kappa}}, \quad b = 4, 8,$$

where a = 0, 1, 2, 3 and b = 4 correspond to the medium I (with superscript I), with b = 5 to 8 to the medium II (with superscript II). After solving the linear system, we obtain the following R/T coefficients calculated by the complex wavenumber k_a (or k_b),

$$R_a = \frac{A_a}{A_0}\frac{k_a}{k_0} = |R_a| \exp(i\vartheta_a), \; a = 1,2.3,4,$$

$$T_b = \frac{A_b}{A_0}\frac{k_b}{k_0} = |T_b| \exp(i\vartheta_b), \; a = 5,6,7,8, \tag{21}$$

where $|R_a|$ and $|T_b|$ denote the R/T amplitudes and ϑ_a and ϑ_b are the corresponding phase angles.

OLKARIA GEOTHERMAL RESERVOIRS

Figure 2a shows the high-temperature geothermal belt in the East African Rift. It is a typical rift-volcanic system. A series of geothermal systems are distributed along the Kenya Rift Valley, where the Olkaria geothermal field, located in the southern end, is considered to be one of the most promising with a total heating area of about 100 km^2 and a thermal storage depth of 500-3000 m (Omenda, 1998). According to the tectonic location, the field can be divided into eastern, northeast, western, and dome regions (see Figure 2b). The field has the highest heat storage temperature in Kenya, with an average temperature of 240 °C and a maximum recorded temperature of 370 °C (Zhang et al., 2018).

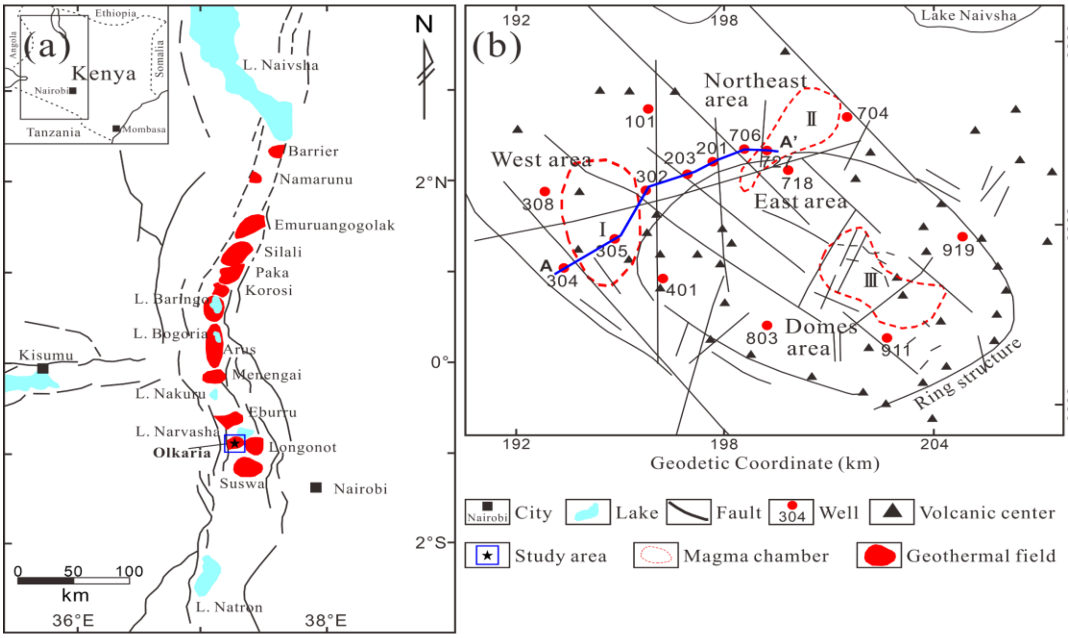

Figure 2. Map of the high-temperature geothermal belt in the Kenya Rift Valley (a) and the Olkaria geothermal field (b) (modified from Zhang et al., 2018).

Geological setting

According to the drilling information and physico-chemical exploration, the Olkaria system is mainly associated with intense volcanic activities in the Late Quaternary (Omenda, 1998). Intense tectonic activities in the East African Rift result in frequent magma intrusions, volcanic activities and fracture networks. Deep rifts, as the upwelling channels of mantle heat flow, control the distribution of heat sources together with shallow faults (Karingithi et al., 2010). As shown in Figure 3, the thermal storage is distributed below 1500 m above the sea level with an effective area of 42 km^2.

The stratigraphic sequence of the Olkaria geothermal field is composed of several typical formations (Rop et al., 2018). Volcanism is normally observed on the surface, including comenditic lavas, pyroclacts, basalts, trychytic intercalations, and volcanic ash. The second layer are Olkaria basalts that consist of basaltic flows, trachytes and minor pyroclasts. It occurs at a depth of approximately 500-1000 m below the ground, acting as cap rocks widespread with low permeability and undeveloped fractures. Plateau trachytes form the third layer at a depth of 1000-1600 m, with major rock types being trachytes with minor occurrence of basalts, tuffs and rhylotes. The layer is deepest in the east field and believed to be related to fissure eruptions along the rift. Mau tuffs are encountered in the fourth layer, which mostly occur in the western field that has been compacted by overburden with ignimbrite texture (Omenda, 1998). The lowest layer is composed mainly of trachytes.

The pressure regime of the formations, measured from wells, serves as the base for such a natural EGS (Ofwona, 2002). Low-pressure zones are in the central and northwest corner and high-pressure zones occur in the eastern and western sides. The low-pressure zone in the center coincides with the low temperature and high resistivity zone and is also a zone of high steam loss from fumaroles. The high-pressure zones coincide with upflow zones recharging the system.

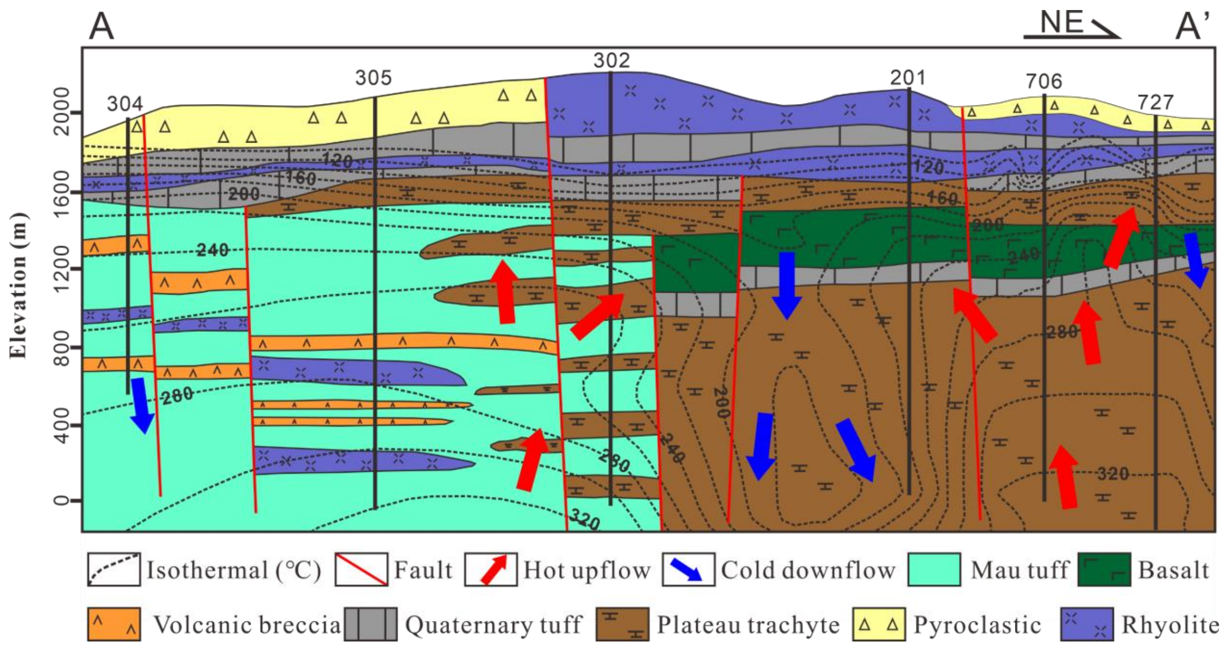

Figure 3. Connected wells' lithology and temperature profile of the Olkaria geothermal field (A-A’ indicated by a blue line in Figure 2b). The thermal storage lithologies are dominated by tuff in the western area and by trachyte in the eastern region. (modified from Shi et al., 2021).

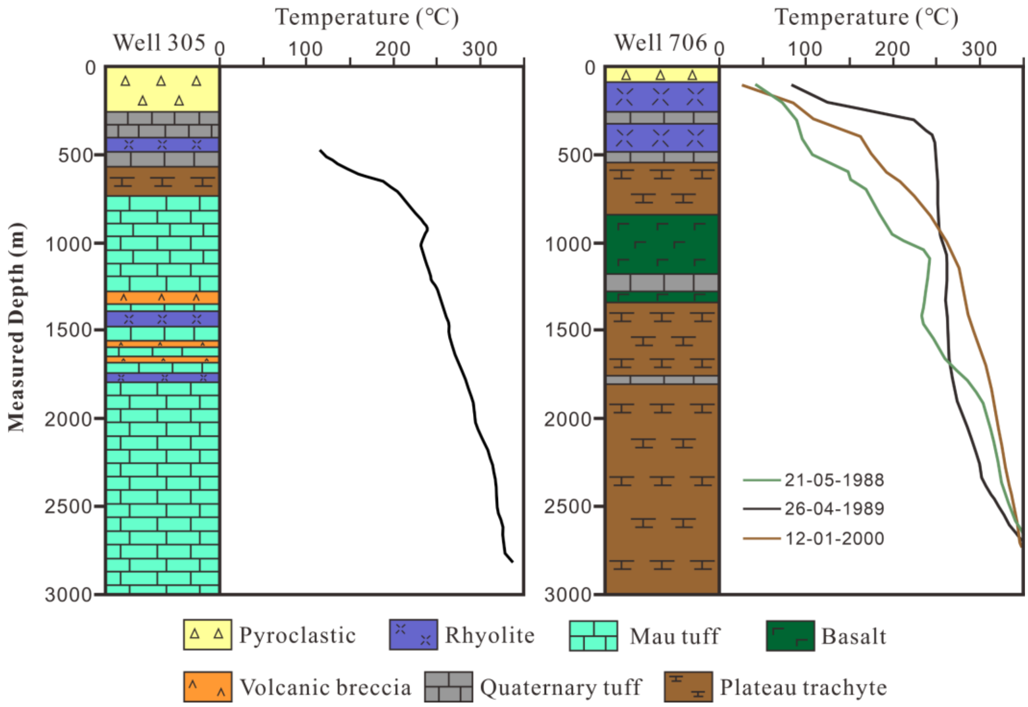

Figure 4. Temperature logs and lithological columns of Well 706 (left) and Well 305 (right). For Well 706, different curves indicate the measurement time. The original temperature data are from Shi et al. (2021).

Geothermal water comes mainly from atmospheric precipitation along the major fractures and partly from infiltration. The reservoir and the transport of fluids in the fractured zone are mainly controlled by faults and cracks in the shaft of the rift valley (Shi et al., 2021). Fluids are mainly stored and transported in broken zones and structural fractures in the form of a high-temperature thermal storage belt. The development of fractures determines the thermal reservoir capacity. From the production point of view, the wells in the north-south direction have similar reservoir characteristics, whereas the wells in the east-west direction, even only 300 m apart, present very large differences in water output. From Figure 3, we see that fractures operate as a channel of cold downflow seepage on the west side of Well 201, but become a heat upwelling channel on the east side. Temperature varies greatly over short distances.

Characteristics of the reservoirs

Drilling reveals two sets of high-temperature reservoirs in the area (Mwaura and Kada, 2017). The first set is located 500 m underground with an average temperature of 235 °C and a thickness above 500 m. The second set is located 2000 m underground with a temperature above 310 °C (Zhang et al., 2018). Figure 4 shows the lithology and temperature profiles of two wells in the western (Well 305) and eastern (Well 706) zones. The geothermal reservoirs are mainly tuff in the west and trachyte in the east. Temperature logs indicate that the shallow layer has a high temperature gradient, which can reach 0.35 °C/m, whereas the deep layer temperature increases slowly, with an average gradient of 0.075 °C/m. The temperature gradient in the eastern part of the study area is slightly higher than that in the western part. The temperature curves of Well 706 show marked changes in different ages. As the hydrothermal rising channel, the formation temperature increases slightly with time.

The reservoir and transport of fluids, apart from the fractured zone, are mainly controlled by petrophysical properties. The thermal storage tuffs in the western region usually have high permeability with original pores and fractures, but are also sensitive to hydrothermal alteration that causes geothermal reservoirs being filled with secondary minerals. The resulting strong heterogeneity in porosity makes the production capacity of adjacent wells very different. The ability to store fluids in the eastern region depends on the degree of development of secondary fissures in the thermal-storage trachytes. In addition, the native cold shrinkage joints of trachytes are also an important channel for fluid storage and transportation. Thermo-poroelastic AVO effects of dissimilar porosities and fluids in the western and eastern regions are important for the seismic monitoring of fluid distributions in these regions.

The properties of pore fluids in the reservoirs are affected by several factors. In such high-temperature environments, the transition of water to vapor phases depends on the pressure condition of the formations, where high pressures tend to keep the water in the liquid phase. Formation boiling curves are often used to describe the critical temperature for the transition of water to vapor phases, where the high-temperature water becomes steam for formation temperatures higher than the boiling one. Figure 5 shows the temperature profiles of several wells in the Olkaria area and the associated boiling curve that starts at 100 °C and maintains a high temperature gradient. We see that the formation temperatures are close to the boiling curve in the shallow zone (<500 m) and become lower with increasing depths. Even for the well with a high geothermal gradient (Figure 5c), the formation temperatures cannot reach the boiling temperature at a depth of 1500 m. Therefore, there are two sets of thermal reservoirs in the Olkaria area, which have different pore-fluid properties. The shallow reservoir with a high geothermal gradient is characteristic of high-temperature water vapor, whereas the deep reservoir with a low geothermal gradient contains high-temperature liquid water.

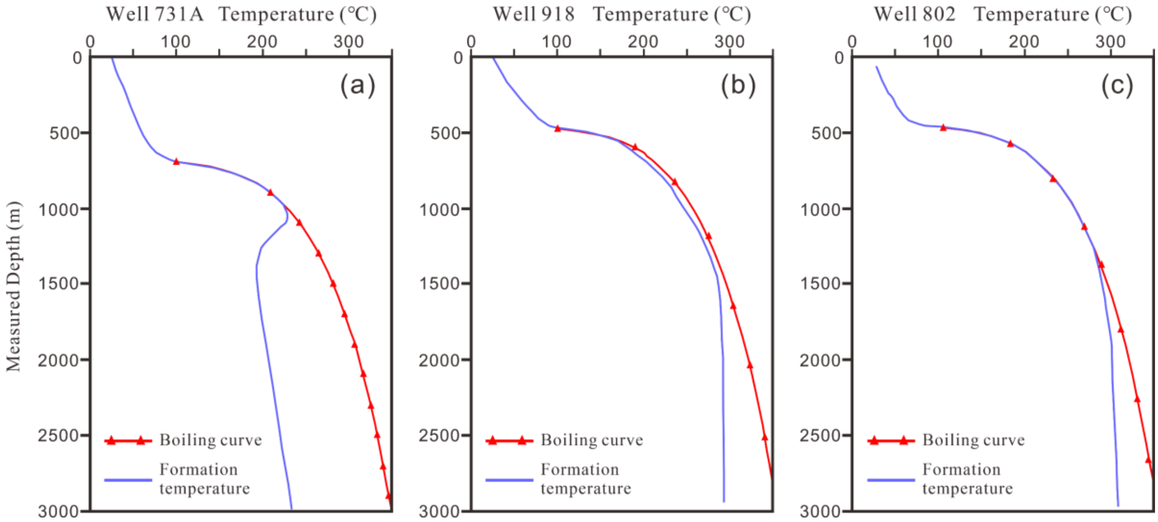

Figure 5. Temperature profiles of three wells in the Olkaria geothermal field (well locations are shown in Figure 2b). The red line is the boiling curve and the blue line is the formation temperature. (modified from Rop, 2013).

It is worth mentioning that geophysical data, including gravity, magnetics, magnetotellurics, transient electromagnetics, and microseismics, have played a vital role in improving the conceptual model of the Olkaria geothermal system over the past decades (e.g., Mariita, 2011; Axelsson et al., 2013; Rop, 2013; Wanjohi, 2014). For example, microseismic data collected in the area from 1996 to 1998 have provided highly valuable S-wave attenuation (Simiyu, 2000; Simiyu and Keller, 2000) to locate several large magma chambers at a depth of ~6 km beneath the Olkaria dome, northeast, and west production fields (see Figure 2b). Intense microseismic activities are usually associated with high-temperature areas near the Quaternary volcanic centers, where the S-wave attenuation derived from microseismic data is sensitive to partially molten material (Carcione et al., 2020). Seismic AVO techniques are believed to be an effective tool for fracture prediction and fluid identification of thermal reservoirs if reflection data are available. To this purpose, we develop a thermo-poroelastic AVO method to simulate the AVO response of geothermal reservoirs. We build a practical model based on previous researches of geothermal reservoirs in the Olkaria area.

RESULTS

The Olkaria geothermal system consists of many seismic reflection layers, as shown in Figure 3. The thermo-poroelastic AVO responses from these layers obtained from angular-trace gathers are used to predict temperature and fluid type. Moreover, the amplitude versus offset and azimuth (AVOA) responses from these layers can be used to estimate the density and orientation of fractures if high-density 3D seismic data are available. The AVOA technique has been widely used for the prediction of fractures, porosity and fluids in oil/gas exploration. In this study, we develop a thermo-poroelastic AVO approach for geothermal reservoirs.

Conceptual petrophysical model

The AVO approach is based on the R/T coefficients (see Figure 1). An accurate model, with detailed lithological, petrophysical and thermophysical properties, and their spatial-time distributions, has not yet built for the Olkaria system. However, some preliminary models have been established by previous studies based on multidisciplinary and well-logging data. For instance, Axelsson et al. (2011) specify parameter ranges for a preliminary volumetric resource assessment of the system where the the petrophysical properties are: rock porosity: 0.05-0.15, rock density (kg/m^3): 2500-2900, rock heat capacity (J/kg°C): 800-1000, water density (kg/m^3): 700-800, and water heat capacity (J/kg°C): 4800-6200. According to the porosity-permeability relationship of trachyte, a porosity of 0.05-0.15 corresponds to average an permeability of 0.1-1 mD (Wang et al., 2015). The cap rock permeability is generally small, and can be set equal to 0.1 mD. Microseismic activities in this area are usually intense in places with high temperatures, especially near the Quaternary volcanic centers. Microseismic data collected by Simiyu (2000) were used to infer the average velocities of different-depth formations in the reservoirs: V_P=2.8 km/s and V_S=1.65 km/s at 0.6 km, 3.9 km/s and 2.28 km/s at 1.5 km, and 4.7 km/s and 2.66 km/s at 4 km.

Based on detailed lithologic compositions (Rop et al., 2018) of stratigraphic sequences, as shown in Figure 4, we determine the elastic and thermophysical properties (Fu, 2019). It is worth noting that the elastic moduli of volcanic rocks decrease approximately linearly with increasing temperature (below 500 °C) because of the decrease of rock strength as well as the generation of microcracks induced by thermal damage (Zhao et al., 2019). As for the properties of pore fluids, based on the comparison of temperature and boiling curves (Figure 5), we assume that the pore fluid in shallow reservoirs is vapor, while the deep reservoirs contain high-temperature water. In this study, we consider the trachyte geothermal reservoirs in the eastern field as an example. This system includes a shallow steam zone and deep boiling water zone, with the reservoir capped by fluid-saturated basalts. Trachyte, as a kind of neutral volcanic ejection rocks with alkali-rich characteristics, is mainly composed of potassium feldspar.

The elastic and thermophysical properties of trachyte are provided by Robertson (1988) and Germinario et al. (2017). The upper and lower media of an interface for thermo-poroelastic AVO modeling are set as basaltic trachyte and plateau trachyte, respectively. The upper medium I serves as low-temperature caprocks with small porosity, specific heat capacity and thermal conductivity, whereas the lower medium II acts as high-temperature reservoir rocks with slightly higher elastic moduli, density and permeability. Table 1 shows the model properties.

Table 1. Petrophysical model. The upper medium I serves as a drained water-saturated caprocks with low-temperature basaltic trachytes, whereas the lower medium II acts as the drained steam-saturated reservoirs with high-temperature plateau trachytes.

Property	Value
Grain bulk modulus, $K_s^{\mathrm{I}}/K_s^{\mathrm{II}}$	40/45 GPa
density, $\rho_s^{\mathrm{I}}/\rho_s^{\mathrm{II}}$	2750/2850 kg/m^3
Frame bulk modulus, $K_m^{\mathrm{I}}/K_m^{\mathrm{II}}$	10/12 GPa
shear modulus, $\mu^{\mathrm{I}}/\mu^{\mathrm{II}}$	11/13 GPa
porosity, $\phi^{\mathrm{I}}/\phi^{\mathrm{II}}$	0.05/0.10
permeability, $\kappa^{\mathrm{I}}/\kappa^{\mathrm{II}}$	0.1/0.8 mD
tortuosity, $\iota^{\mathrm{I}}/\iota^{\mathrm{II}}$	2/2

absolute temperature, $T^{\mathrm{I}}/T^{II}_{(steam)}$	100/120 °C
absolute temperature, $T^{\mathrm{I}}/T^{II}_{(liquid)}$	280/300 °C
Water density, $\rho_f^{\mathrm{I}}/\rho^{\mathrm{II}}_{f(steam)}$	600/600 kg/m^3
Water density, $\rho_f^{\mathrm{I}}/\rho^{\mathrm{II}}_{f(liquid)}$	820/810 kg/m^3
viscosity, $\eta_f^{\mathrm{I}}/\eta^{\mathrm{II}}_{f(steam)}$	0.015/0.015 mPa s
viscosity, $\eta_f^{\mathrm{I}}/\eta^{\mathrm{II}}_{f(liquid)}$	1/1 mPa s
Bulk specific heat, $C_e^{\mathrm{I}}/C_e^{\mathrm{II}}$	320/820 kg/(m s^2 °C)
thermoelasticity coefficient, $\beta^{\mathrm{I}}/\beta^{\mathrm{II}}$	$1.2/2.4\ 10^6$kg/(m s^2 °C)
thermal conductivity, $\gamma^{\mathrm{I}}/\gamma^{\mathrm{II}}$	1/1.9 m kg/(s^3 °C)
relaxation time, $\tau^{\mathrm{I}}/\tau^{\mathrm{II}}$	$1.5 \times 10^{-8}/1.5 \times 10^{-8}\ s$

Velocity dispersion and attenuation

In this section, we analyze the dispersion and attenuation of waves in medium II (see Table 1), based on the dispersion Eq. (6). Frequency-dependent phase velocities and dissipation coefficients are calculated to illustrate the effect of thermal conductivity, specific heat, and porosity on the fast P, Biot slow P, and thermal slow P waves.

Thermal conductivity is the most important property, which characterizes the heat-transfer capability of the rock. It depends not only on the mineral composition, but also on their distribution, shape, internal structure, temperature etc. Figure 6 compares the velocities and dissipation coefficients of the fast P, Biot slow P, and thermal slow P waves for the thermal conductivities: 1.9, 3.2, and 4.5 m·kg/(s^3·°C). We can see two inflection points in the fast P-wave velocity, which correspond to the Biot and thermal peaks in the attenuation plot (Figures 6a and 6b). The Biot peak is caused by friction between the fluid and the grains (Biot, 1956) and hardly depends on the thermal conductivity. In general, there are no variations in the low-frequency range. The attenuation peak strength increases significantly with increasing thermal conductivity, at high frequencies. The Biot slow P-wave follows a similar behavior (Figures 6c and 6d), while the thermal slow P-wave velocity increases slightly (Figures 6e and

6f).

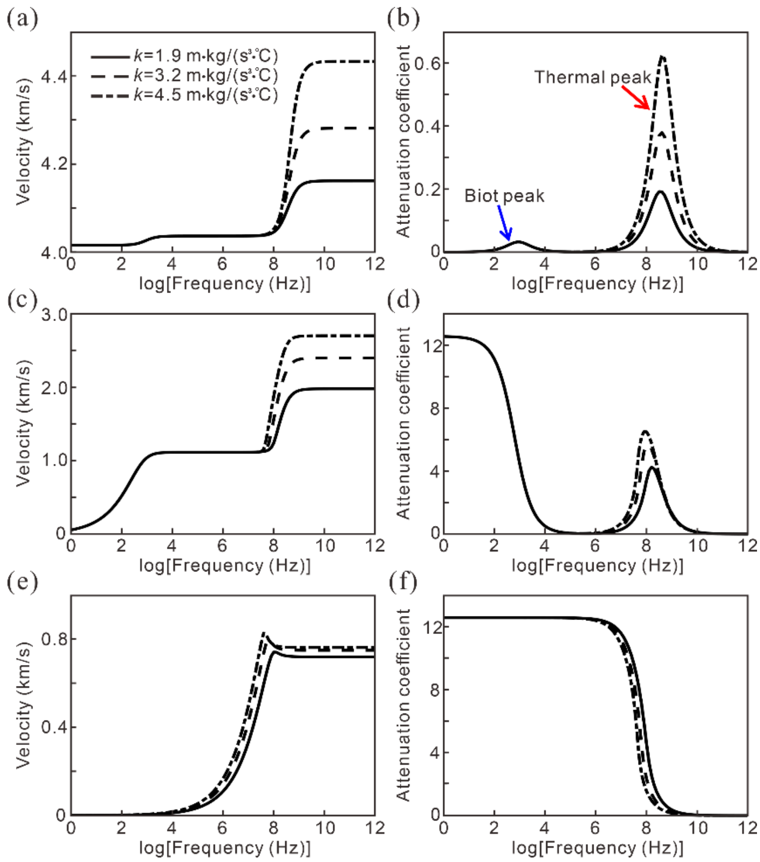

Figure 6. Phase velocities (a, c, and e) and dissipation coefficients (b, d, f) as a function of frequency for the fast P (a, b), Biot slow P (c, d), and thermal slow P (e, f) waves at different thermal conductivities. The other properties are listed in Table 1.

Specific heat is the amount of heat absorbed or released per unit mass under temperature variations. At the same temperature, a reservoir with a high specific heat stores more heat energy. Figure 7 compares the velocities and dissipation coefficients of the fast-P, Biot slow-P, and thermal slow-P waves for the specific heats: 820, 920, and 1020 kg/(m·s^2·°C). We see that the fast-P velocity is highly affected, increasing with decreasing specific heat, while the Biot and thermal peaks show slight changes. The specific heat of rocks is attributed to lattice vibrations and particle thermal motion. Particularly, these vibrations become dominant at high temperatures and therefore, affect the fast-P velocity.

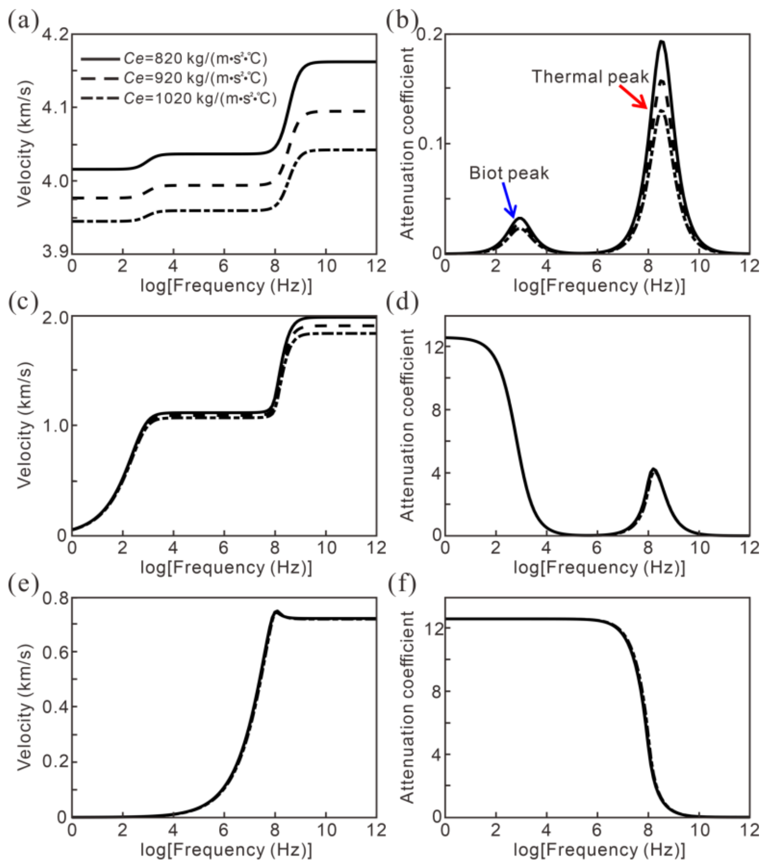

Figure 7. Phase velocities (a, c, and e) and dissipation coefficients (b, d, f) as a function of frequency for the fast P (a, b), Biot slow P (c, d), and thermal slow P (e, f) waves at different specific heats. The other properties are listed in Table 1.

Figure 8 compares the phase velocities and dissipation coefficients of the fast P, Biot slow P, and thermal slow P waves for the porosities: 0.05, 0.10, and 0.15. As expected, the fast-P velocity significantly decreases with increasing porosity. High temperatures obviously enhance the effect over room temperatures due to decreased strength of rocks. The Biot attenuation moves to higher frequencies, whereas the thermal attenuation increases with increasing porosity. Dispersion occurs at frequencies (10^3~10^8 Hz) and higher than 10^8 Hz for the Biot slow-P and thermal slow-P waves, respectively.

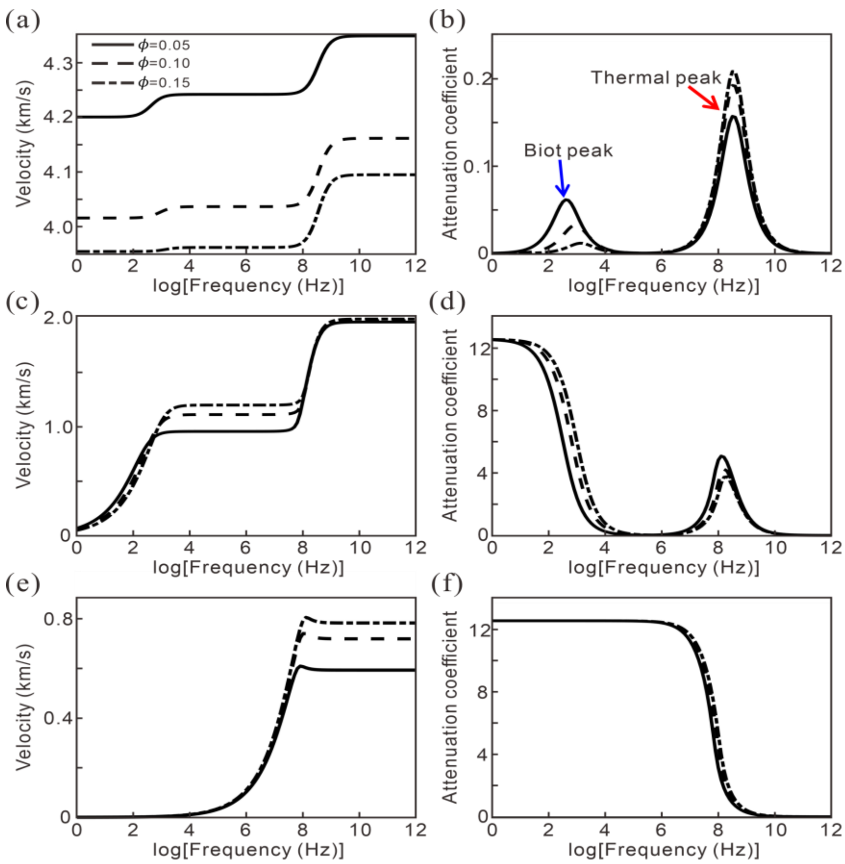

Figure 8. Phase velocities (a, c, and e) and dissipation coefficients (b, d, f) as a function of frequency for the fast P (a, b), Biot slow P (c, d), and thermal slow P (e, f) waves at different porosities. The other properties are listed in Table 1.

AVO modeling

Next, we investigate the angle-dependent R/T responses to temperature, porosity, specific heat, and fluid type in the case of an incident P wave. Eq. (21) gives the reflection and transmission coefficients of the fast-P wave (R_{P1}, T_{P1}), slow-P wave (R_{P2}, T_{P2}), T wave (R_{PT}, T_{PT}) and S wave (R_{PS}, T_{PS}).

Figure 9 shows the coefficients with the upper/lower media temperatures of 100 °C/120 °C, 280 °C/300 °C, and 360 °C/380 °C, which represent a shallow steam zone (500 m), a deep boiling water zone (1500 m), and a deeper high temperature zone (3000 m) of the Olkaria geothermal system, respectively. As expected, the fast P wave (R_{P1}, T_{P1}) and T wave (R_{PT}, T_{PT}) reflections shows small variations below the critical angle, with small amplitudes, because of the small impedance contrast between trachyte caprocks and trachyte reservoirs, whereas higher values occur beyond the critical angle, especially for supercritical cases. R_{P2} decreases with increasing incidence angles. The S wave (R_{PS}, T_{PS}) shows similar characteristics to the case of thermoelasticity (Hou et al., 2022a). We conclude that different temperature conditions affect the critical angle and intercept of the AVO response. The two cases with deep temperature conditions with boiling water show large differences compared to the shallow temperature one with steam. It can be shown that the angle-dependent R/T coefficients are consistent with the conservation of energy (Hou et al., 2022d). These AVO can be the foundation for the seismic interpretation of reflection amplitudes from thermo-poroelastic media.

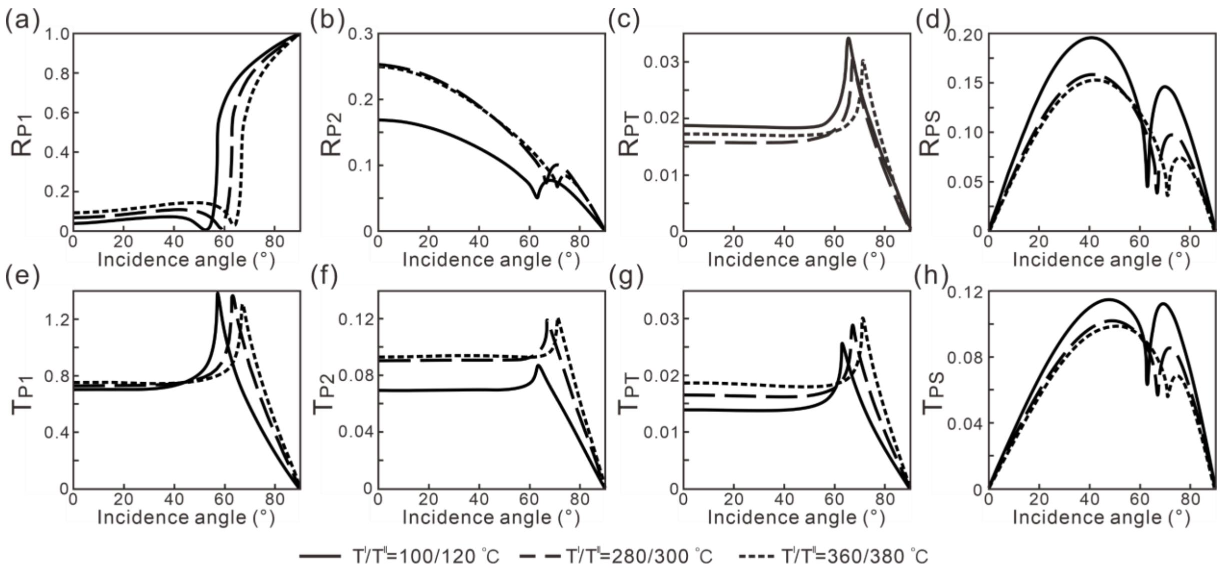

Figure 9. Reflection (a, b, c, d) and transmission (e, f, g, h) amplitudes as a function of the P-wave incidence angle at different conditions with upper/lower media temperatures of 100 °C/120 °C, 280 °C/300 °C, and 360 °C/380 °C. The properties are listed in Table 1.

Trachyte thermal reservoirs usually have a low porosity that is mainly controlled by tectonic factors and has a great influence on the petrophysical properties and fluid distribution of thermal reservoirs. Figure 10 shows the coefficients of the deep reservoir with boiling water, where the porosity (ϕ^{II}) takes the values 0.05, 0.1, and 0.15, with the other properties constant as given in Table 1. We see that increasing of ϕ^{II} reduces the modulus difference between caprock and reservoir, thus reducing the intercept and gradient of R_{P1} and R_{P2}, and enhancing the transmission energy of these waves, and the critical angle has increased from 50° to 65°. The T wave (R_{PT}, T_{PT}) is angle independent below the critical angle, but significant changes occur above this angle. Both, T_{P2} and $T_{PT,}$ show large discrepancies at the different porosities.

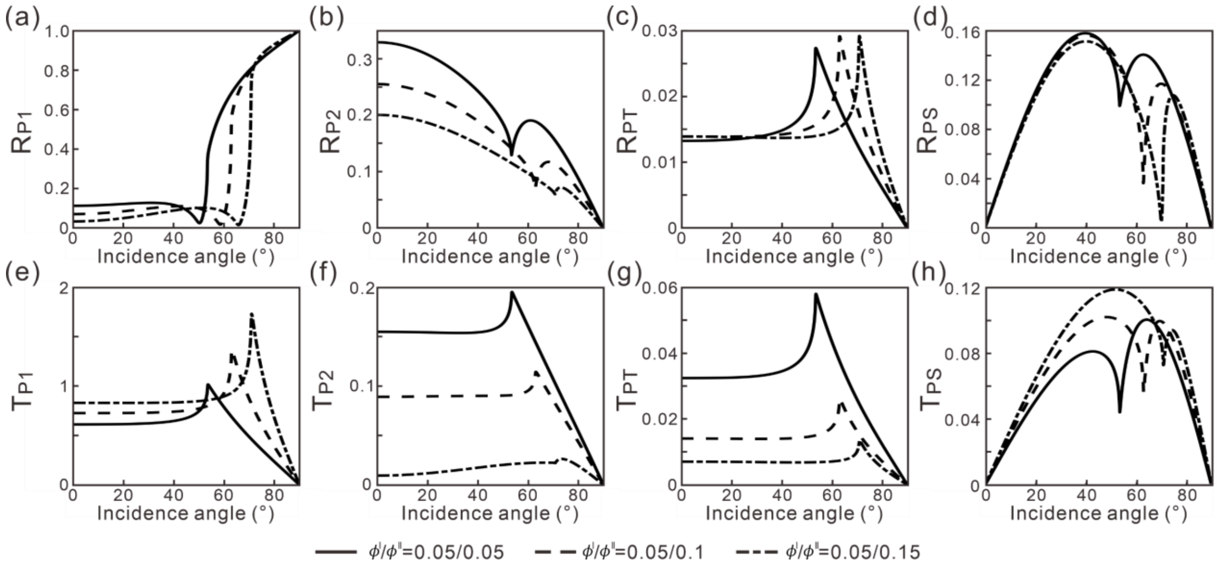

Figure 10. Reflection (a, b, c, d) and transmission (e, f, g, h) amplitudes as a function of the P-wave incidence angle for the deep reservoir with boiling water, where the porosity (ϕ^{II}) varies as 0.05, 0.1, and 0.15, with the other properties constant as given in Table 1.

The specific heat affects the heat exchange efficiency of EGS. The aforementioned plane-wave analysis (see Figure 7) indicates that increasing specific heat reduces the fast-P velocity, and fluid- and heat-flow effects. Figure 11 shows the coefficients of the deep reservoir with boiling water, where the specific heat (C_e^{II}) varies as 820, 920, and 1020 kg/(m·s^2·°C), with the other properties constant as given in Table 1. We see that T_{P2} and T_{PT} are sensitive to differences in the specific heat between the caprock and reservoir, whereas the other waves show little variations, also because of the narrow range of specific-heat variations.

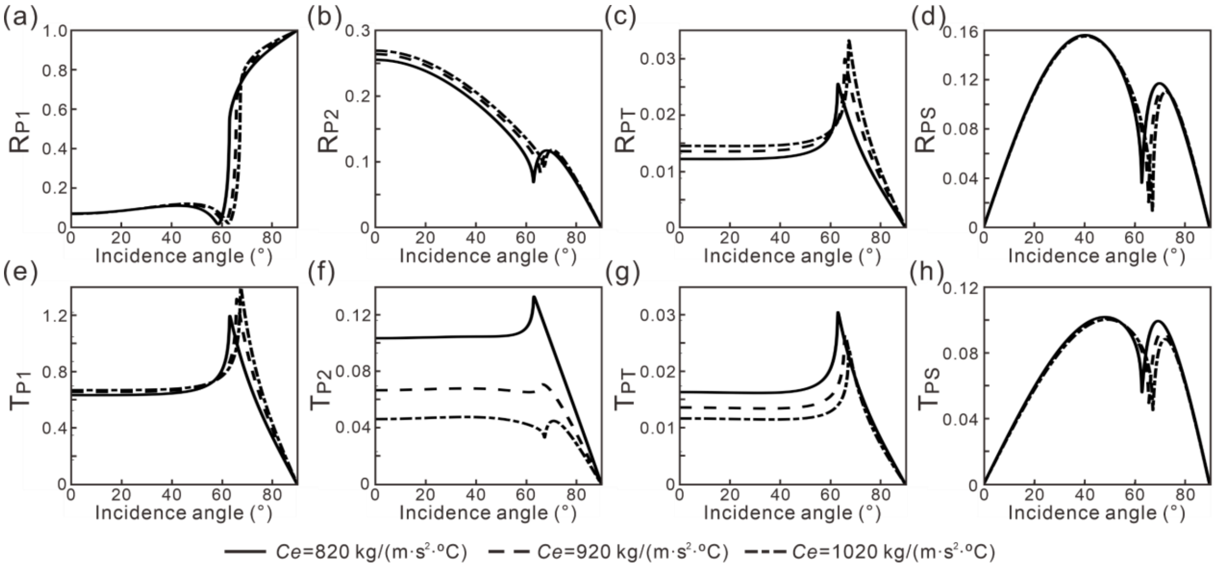

Figure 11. Reflection (a, b, c, d) and transmission (e, f, g, h) amplitudes as a function of the P-wave incidence angle for the deep reservoir with boiling water, where the specific heat (C_e^{II}) varies as 820, 920, and 1020 kg/(m·s^2·°C), with the other constant as given in Table 1.

In AVO inversion of seismic data, the fast-P reflection coefficient (R_{P1}) is the most useful. The calculations show that, in this specific case, R_{P1} slightly increases with angle, with a sharp increase beyond the critical angle. In addition to the above properties, pore fluids also have affected the AVO response. Supercritical CO_2 ($SCCO_2$) has a liquid density and a gaseous viscosity, with a diffusion coefficient much higher than that of water. Therefore, $SCCO_2$ can replace water as a heat transfer fluid for EGS (Cao et al., 2016). Next, we compare the AVO responses of thermal reservoirs saturated by water, $SCCO_2$ and gas. We consider: water: ρ_f= 820 kg/m^3, η_f= 0.001 Pa s, and β_f = 40000 kg/(m s^2 °C); gas: ρ_f = 1.21 kg/m^3, η_f=1.79*10^{-7} Pa s, and β_f = 60000 kg/(m s^2 °C); and $SCCO_2$: ρ_f = 700 kg/m^3, η_f = 4*10^{-5} Pa s, and β_f = 50000 kg/(m s^2 °C)。

Figure 12 shows the coefficients of the deep reservoir saturated by water, $SCCO_2$, and gas (dry case), where we can see quite different behaviors depending on the type of fluid. For instance, supercritical CO_2 induces a larger critical angle than that of water. As expected, the gas-saturated reservoir has a higher reflection coefficient, gradient, intercept, and critical angle. It is possible to use these coefficients to monitor whether the heated water enters the intended channel in the EGS. Therefore, seismic monitoring of EGSs could analyze fluid paths (water or dry) of fractures and further evaluate the quality of hydrofracturing, which is important for EGSs because many of them fail due to fluid leakage or short circuits.

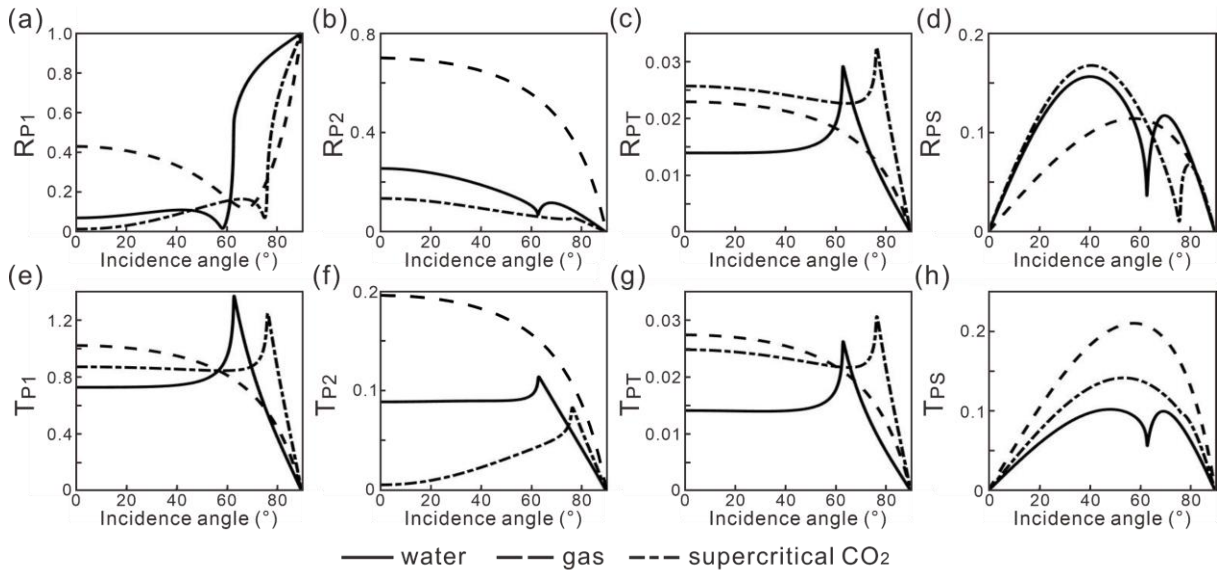

Figure 12. Reflection (a, b, c, d) and transmission (e, f, g, h) amplitudes as a function of the P-wave incidence angle for the deep reservoir saturated by water, $SCCO_2$, and gas (dry case), with the other properties constant as given in Table 1.

To show how to identify fluids, we calculate the Russell fluid factor (Russell et al., 2003) and intercept gradient (PG) for the deep reservoir saturated with different fluids. The fluid factor is $F = I_P^2 - cI_S^2$ where I_P and I_S are the intercept and gradient values of AVO curve, and coefficient $c = (V_P/V_S)_{dry}^2 = 2.24$ is the square of the dry rock velocity ratio of longitudinal and transverse wave (see Table 1). Figure 13 shows the crossplot of F and PG, where we can see that the crossplot can clearly discriminate between different fluids. The ordinate is normalized for the sake of observation. Dry rocks exhibit a negative PG value and a very low fluid factor, whereas water as a heat recovery fluid leads to a positive PG value and a high fluid factor. As expected, the AVO response to $SCCO_2$ lies somewhere between water and gas because of its liquid density and gaseous viscosity. Then, these crossplots could be used to identify the distribution of hydrofracturing networks and further determine whether the heat recovery fluid (water or $SCCO_2$) enters the expected channel in the EGS.

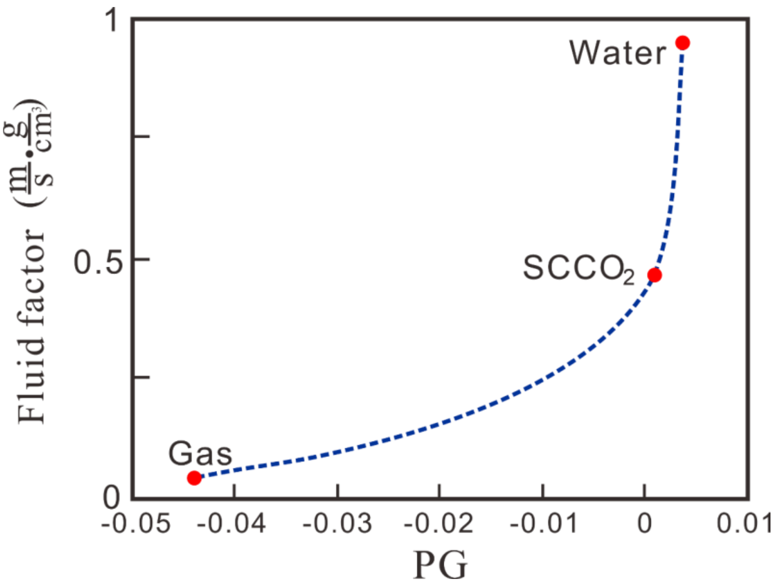

Figure 13. Crossplot of Russell fluids factors (*F*) and PG values for the deep reservoir saturated with water, $SCCO_2$, and gas (dry case), with the other properties constant as given in Table 1.

CONCLUSIONS

Seismic AVO is one method for the exploration and development of geothermal resources. It has the potential to enable a time-lapse reflection seismic monitoring of enhanced geothermal systems by identifying the fluid distribution across hydrofracturing networks. Conventional AVO techniques cannot be directly applied to thermal reservoirs because they do not consider the thermal properties. To this purpose, we develop a thermo-poroelastic AVO theory, where P-wave incidence generates reflected and transmitted fast-P, Biot slow-P, thermal slow-P, and S waves.

We consider, as an example, the Olkaria geothermal reservoirs in Kenya, where the transition of water to vapor phases depends on both the temperature and pressure conditions in the upflow zone. Based on lithological, petrophysical, and thermophysical properties of the trachyte thermal reservoirs in the eastern field, we build a conceptual interface model to obtain the R/T coefficients, essential to perform AVO modeling. The conditions considered represent the shallow steam zone, the deep boiling water zone, and the deeper high temperature zone.

First, a plane-wave analysis illustrates the effects of thermal conductivity, specific heat, and porosity on the velocity and attenuation of the different waves. For temperatures less than

400°C, limited changes in the thermophysical properties (e.g., thermal conductivity and specific heat) induced by non-lithologic factors (e.g., microstructure and temperature) hardly affect the velocity and attenuation at seismic frequencies, whereas porosity has a pronounced effect, as it is well known.

Then, we analyze the effects of temperature, porosity, specific heat and fluid type in the case of P-wave incidence, which significantly affect the critical angle. Deep high-temperature conditions with boiling water show large discrepancies compared to shallow low-temperature conditions with steam. Increasing porosity reduces the intercept and gradient of the P-wave AVO response. The fluid type has the most pronounced effect, which makes AVO technique useful to detect fluids. In fact, water, $SCCO_2$, and gas (dry case), as heat transfer fluids, show distinct characteristics. Finally, it is shown how a crossplot of intercept gradient/fluid factor can be used as a precursor for fluid identification.

ACKNOWLEDGEMENTS

The research is supported by the National Natural Science Foundation of China (Grant Nos. 42230803, 41821002) and 111 project "Deep-Superdeep Oil & Gas Geophysical Exploration" (B18055).

REFERENCES

Axelsson, G., Arnaldsson, A., Árnason, K., Franzson, H., Fridriksson, Th., Gylfadóttir, S.S., Halldórsdóttir, S., Hólm, S., 2011. Preliminary assessment of the electrical generating capacity of the greater olkaria geothermal system. KenGen-report, Olkaria.

Axelsson, G., Arnaldsson, A., Armannsson, H., Árnason, K., Einarsson, G., Franzson, H., Fridriksson, T., Gudmundsson, G. etc., 2013, Updated conceptual model and capacity estimates for the greater olkaria geothermal system, Kenya. In: Proceedings of the 38th Workshop on Geothermal Reservoir Engineering. Stanford University, California, SGP-TR-198, pp. 1–16.

Ba, J., Carcione, J. M., and Nie, J. X., 2011. Biot-Rayleigh theory of wave propagation in double-porosity media: Journal of Geophysical Research. Solid Earth. 116, B06202. https://doi.org/10.1029/2010JB008185.

Baldonedo, J., Bazarra, N., Fernández, J. R., and Quintanilla, R., 2020. An a priori error analysis of a Lord-Shulman poro-thermoelastic problem with micro temperatures. Acta Mechanica. 231, 4055–4076. https://doi.org/10.1007/s00707-020-02738-z.

Batzle, M. L., and Wang, Z., 1992. Seismic properties of pore fluids. Geophysics. 57(11), 1396–1408.

https://doi.org/10.1190/1.1443207.

Berard, T., and Cornet F. H., 2003. Evidence of thermally induced borehole elongation: a case study at Soultz, France. International Journal of Rock Mechanics and Mining Sciences. 40, no. 7, 1121–1140, https://dx.doi.org/10.1016/S1365-1609(03)00118-7.

Biot, M. A., 1956. Thermoelasticity and irreversible thermodynamics. Journal of Applied Physics. 27, 240–253, doi: 10.1063/1.1722351.

Borcherdt, R. D., 2009. Viscoelastic waves in layered media. Cambridge University Press.

Breede, K., Dzebisashvili, K., Liu, X., and Falcone, G., 2013. A systematic review of enhanced (or engineered) geothermal systems: past, present and future. Geothermal Energy. 1, no. 1, 1–27, https://dx.doi.org/10.1186/2195-9706-1-4.

Cao, W. J., Huang, W. B., and Jiang, F. M., 2016. Numerical study on variable thermophysical properties of heat transfer fluid affecting EGS heat extraction. International Journal of Heat and Mass Transfer. 92, 1205–1217. doi: 10.1016/j.ijheatmasstransfer.2015.09.081.

Carcione, J. M., Poletto, F., Farina, B., and Bellezza, C., 2018. 3D seismic modeling in geothermal reservoirs with a distribution of steam patch sizes, permeabilities and saturations, including ductility of the rock frame. Physics of the Earth and Planetary Interiors. 279, 67–78. doi: 10.1016/j.pepi.2018.03.004.

Carcione, J. M., Cavallini, F., Wang, E. J., Ba, J., and Fu, L.-Y., 2019. Physics and Simulation of Wave Propagation in Linear Thermo-poroelastic Media: Journal of Geophysical Research. Solid Earth, 124, 8147–8166. doi: 10.1029/2019JB017851.

Carcione, J. M., Farina, B., Poletto, F., Qadrouh, A. N., and Cheng, W., 2020. Seismic attenuation in partially molten rocks, Physics of the Earth and Planetary Interiors, https://doi.org/10.1016/j.pepi.2020.106568

Chen, J. S., Hoversten, G. M., Key, K., Nordquist, G., and Cumming, W., 2012. Stochastic inversion of magnetotelluric data using a sharp boundary parameterization and application to a geothermal site. Geophysics. **77**, no.4, E265–E279. doi: 10.1190/GEO2011-0430.1.

Colwell, C., Wijk, K. V., and Liberty, L., 2012. Integrated geophysical exploration of a known geothermal resource. Neal Hot Springs: SEG Las Vegas 2012 Annual Meeting, 1–5, doi: 10.1190/segam2012-1543.1.

Fawad, M., Hansen, J. A., Mondol, N. H., 2020. Seismic-fluid detection-a review. Earth-Science Reviews. 210, 103347. https://doi.org/10.1016/j.earscirev.2020.103347.

Fu, L.-Y., 2019. Geophysical characterization of Olkaria geothermal reservoirs in Kenya. Tech. Report, BGPYJY2017-963: CNPC Greatwall Drilling Engineering Company Ltd.

Germinario, L., Siegesmund, S., Maritan, L., and Mazzoli, C., 2017. Petrophysical and mechanical properties of Euganean trachyte and implications for dimension stone decay and durability performance. Environ Earth Sci. 76, 739–760. doi: 10.1007/s12665-017-7034-6.

Guitton, W. T., 2020. The value of geophysical data for geothermal exploration: Examples from empirical, field, and synthetic data. The Leading Edge. 39, no. 12, 864–872. doi: 10.1190/tle39120864.1.

Hou, W.T., Fu, L.-Y., Carcione, J.M., Wang, Z.W., and Wei, J., 2021. Simulation of thermoelastic waves based on the Lord-Shulman theory. Geophysics. 86, T155–T164. https://doi.org/10.1190/geo2020-0515.1.

Hou, W.T., Fu, L.-Y., Carcione, J.M., and Han, T.C., 2022a. Reflection and transmission of plane waves in thermoelastic media. Frontiers in Earth Science. 10, 1–16. doi: 10.3389/feart.2022.850331.

Hou, W.T., Fu, L.-Y., and Carcione, J.M., 2022b. Reflection and transmission of thermoelastic waves in

multilayered media. Geophysics. 87, MR117-MR128. https://doi.org/10.1190/geo2021-0542.1.
Hou, W.T., Fu, L.-Y., and Carcione, J.M., 2022c. AVO in thermoelastic media. Geophysics. GEO-2021-0815.
Hou, W.T., Fu, L.-Y., and Carcione, J.M., 2022d. Reflection and transmission of inhomogeneous plane waves in thermo-poroelastic media: in review.
Ignaczak, J., Ostoja-Starzewski, M., 2010. Thermoelasticity with finite wave speeds. Oxford University Press.
Karingithi, C. W., Arnórsson, S., and Grönvold, K., 2010. Processes controlling aquifer fluid compositions in the Olkaria geothermal system, Kenya. Journal of Volcanology and Geothermal Research. 196, 57–76. doi: 10.1016/j.jvolgeores.2010.07.008.
Kent, T., and Louie, J. J., 2013. Correlating azimuthal anisotropy to geothermal resource potential using a 3D-3C seismic survey of Soda Lake geothermal field, Nevada. SEG Houston 2013 Annual Meeting, 341–346. doi: 10.1190/segam2013-1398.1.
Lehujeur, M., Vergne, J., Schmittbuhl, J., and Maggi, A., 2015. Characterization of ambient seismic noise near a deep geothermal reservoir and implications for interferometric methods: a case study in northern Alsace, France. Geothermal Energy. 3, no. 1, 1–17. https://doi.org/10.1186/s40517-014-0020-2.
Li, N. Q., Deng. W. B., Fu. L. Y., Carcione. J. M., and Han. T. C., 2022a. Wave propagation in double-porosity thermoelastic media. Geophysics. 87, MR265-MR277. https://doi.org/10.1190/geo2022-0008.1.
Li, N. Q., Fu, L. Y., Deng, W. B., Carcione, J. M., and Yang, J., 2022b. A thermo-hydro-mechanical model to evaluate the seismic properties of geothermal reservoirs. Geophysics, in review.
Lu, S. M., 2018. A global review of enhanced geothermal system (EGS). Renewable and Sustainable Energy Reviews. 81, 2902–2921. doi: 10.1016/j.rser.2017.06.097.
Lord, H. W., and Shulman, Y., 1967. A generalized dynamical theory of thermoelasticity. Journal of the Mechanics and Physics of Solids. 15, 299–309. doi: 10.1016/0022-5096(67)90024-5.
Mariita, N.O., 2011. Exploration history of olkaria geothermal field by use of geophysics. Presented at Short Course VI on Exploration for Geothermal Resources, organized by UNU-GTP, GDC and KenGen, at Lake Bogoria and Lake Naivasha, Kenya, Oct. 27–Nov. 18, 2011.
Mwaura, D., Kada, M., 2017. Developing a web-based spatial decision support system for geothermal exploration at the Olkaria geothermal field. International Journal of Digital Earth. 10, no. 11, 1118–1145. doi: 10.1080/17538947.2017.1284909.
Nield, D.A. and Bejan, A, 2006. Convection in Porous Media, 3rd ed. Springer.
Noda, N., 1990. Thermal stress problem in a fluid-filled porous circular cylinder. Z. Angew. Math. Mech., 70, 543–549, doi: 10.1002/zamm.19900701203.
Ofwona, C.O., 2002. A reservoir Study of Olkaria East Geothermal System, Kenya. United Nations University, Geothermal Training Programme, Report 1.
Olasolo, P., Juárez, M. C., Morales, M. P., and Liarte, I. A., 2016. Enhanced geothermal systems (EGS): A review. Renewable and Sustainable Energy Reviews. 56, 133–144. https://dx.doi.org/10.1016/j.rser.2015.11.031.
Omenda, P. A., 1998. The geology and structural controls of the Olkaria geothermal system. Kenya.

Geotherm. 27, no. 1, 55–74. doi: 10.1016/S0375-6505(97)00028-X.

Pandey S. N., Vishal V., Chaudhuri A., 2018. Geothermal reservoir modeling in a coupled thermo-hydro-mechanical-chemical approach: A review. Earth-Science Reviews. 185, 1157–1169. https://doi.org/10.1016/j.earscirev.2018.09.004.

Patterson, J. R., Cardiff, M., Coleman, T., Wang, H., Feigl, K. L., Akerley, J., and Spielman, P., 2017. Geothermal reservoir characterization using distributed temperature sensing at Brady Geothermal Field, Nevada. The Leading Edge. 36, no. 12, 962–1044. doi: 10.1190/tle36121024a1.1.

Peacock, J. H., Thiel, S., Heinson, G. S., and Reid, P., 2013. Time-lapse magnetotelluric monitoring of an enhanced geothermal system. Geophysics. 78, no. 3, B121–B130. doi: 10.1190/GEO2012-0275.1.

Poletto, F., B. Farina, and J. M. Carcione, 2018, Sensitivity of seismic properties to temperature variations in a geothermal reservoir: Geothermics, 76, 149–163, https//doi.org/10.1016/j.geothermics.2018.07.001.

Qi, H., Ba, J., and Müller, T. M., 2021. Temperature effect on the velocityporosity relationship in rocks. Journal of Geophysical Research: Solid Earth. 126, 19–27. https://doi.org/10.1029/2019JB019317.

Rathnaweera, T. D., Wu, W., Ji, Y. L., Gamage, R. P., 2020. Understanding injection-induced seismicity in enhanced geothermal systems: From the coupled thermo-hydro-mechanical-chemical process to anthropogenic earthquake prediction. Earth-Science Reviews. 205, 103182. https://doi.org/10.1016/j.earscirev.2020.103182.

Robertson, E. C., 1988. Thermal Properties of Rocks. United States Department of the Interior Geological Survey.

Rop, E., 2013. Interpretation of Recent Temperature and Pressure data and Updated Conceptual Model of Greater Olkaria Geothermal systems, Kenya, North Iceland. UNU Geothermal Training Program, Reykjavik, Iceland. Report 32

Rop, E., Hikari F., and Saeid J., 2018. An updated numerical model of the Greater Olkaria geothermal system, Kenya. PROCEEDINGS, 43rd Workshop on Geothermal Reservoir Engineering Stanford University, Stanford, California, February 12-14, 2018, SGP-TR-213.

Russell, B. H., Hedlin, K., Hilterman, F. J., and Lines, L. R., 2003. Fluid-property discrimination with AVO: A Biot-Gassmann perspective. Geophysics, 68, no. 1, 29–39. doi: 10.1190/1.1543192.

Salaun, N., Toubiana, H., Mitschler, J. B., Gigou, G., Carriere, X., Maurer, V., and Richard, A., 2020. High-resolution 3D seismic imaging and refined velocity model building improve the image of a deep geothermal reservoir in the Upper Rhine Graben. The Leading Edge. 39, no. 12, 857–863. doi: 10.1190/tle39120857.1.

Sharma, M. D., 2008. Wave propagation in thermoelastic saturated porous medium. Journal of Earth System Science. 117, 951–958. doi: 10.1007/s12040-008-0080-4.

Shi, Y. Z., Rop, E., Wang, Z. C., Jiang, G. Z., Wang, S. J., and Hu, S. B., 2021. Characteristics and formation mechanism of the Olkaria geothermal system, Kenya revealed by well temperature data. Geothermics. 97, 1–12. doi: 10.1016/j.geothermics.2021.102243.

Simiyu, S. M., 2000. Geothermal reservoir characterization: application of microseismicity and seismic wave properties at Olkaria, Kenya rift. Journal of Geophysical Research: Solid Earth. 105, no. B6, 13779–13795. doi: 10.1029/1999JB900401.

Simiyu, S. M., Keller, G. R., 2000. Seismic monitoring of the Olkaria Geothermal area, Kenya Rift valley. J. Volcanol. Geotherm. Res 95 (1–4), 197–208. https://doi.org/10.1016/S0377-0273(99)00124-9.

Shuey, R. T., 1985. A simplification of the Zoeppritz equations. Geophysics. 50(4), 609–614. https://doi.org/10.1190/1.1441936.

Vasco, D. W., Rutqvist, J., Jeanne, P., Samsonov, S. V., and Hartline, C., 2020. Using geodetic data in geothermal areas. The Leading Edge. 39, no. 12, 883–892. doi: 10.1190/tle39120883.1.

Wang, P. J., Chen, C. Y., Zhang, Y., Go, Y. F., Qu, X. J., and Yi, J., 2015. Characteristics of volcanic reservoirs and distribution rules of effective reservoirs in the Changling fault depression, Songliao Basin. Natural Gas Industry. 2, no. 12, 440–448. doi: 10.1016/j.ngib.2015.09.020.

Wang, Z.W., Fu, L. Y., Wei, J., Hou, W.T., Ba, J., and Carcione, J.M., 2020. On the Green function of the Lord–Shulman thermoelasticity equations. Geophys. J. Int. 220, 393–403. https://doi.org/10.1093/gji/ggz453.

Wang, E., Carcione, J. M., Yuan, Y., and Ba, J., 2021. Reflection of Inhomogeneous Plane Waves at the Surface of a Thermo-Poroelastic Medium. Geophys. J. Int. 224 (3), 1621–1639. https://doi.org/10.1093/gji/ggaa543.

Wanjohi, A.W., 2014. Geophysical survey of a high-temperature field, Olkaria. In: Proceedings of the Short Course IX on Exploration for Geothermal Resources, Lake Naivasha and Lake Bogoria, Kenya, pp. 1–12. Nov 2–24.

Wei, J., Fu, L. Y., Wang, Z. W., Ba, J., and Carcione, J. M., 2020. Green's function of the Lord–Shulman thermo-poroelasticity theory. Geophysical Journal International. 221, no. 3, 1765–1776. doi: 10.1093/gji/ggaa100.

West-JEC, 2009: The Olkaria Optimization Study (Phase II)–Final reservoir analysis report. West Japan Engineering Consultants, Inc.

Willis, E., Bresee, J., Bona, B. D., Salisbury, J., Mock, J. T., Jelacic, A., Goldman, P., and Mink, L. R., 2010. A History of Geothermal Energy Research and Development in the United States. Geothermal Technologies Program, U.S. Department of Energy.

Yang J., Fu, L. Y., Zhang, W. Q., and Wang, Z. W., 2019. Mechanical property and thermal damage factor of limestone at high temperature. International Journal of Rock Mechanics and Mining Sciences, 117:11–19. https://doi.org/10.1016/j.ijrmms.2019.03.012.

Yang J., Fu, L. Y., Fu, B. Y., Wang, Z. W., and Hou, W. T., 2021. High-temperature effect on the material constants and elastic moduli for solid rocks. Journal of Geophysics and Engineering. 18(4): 583–593. https://doi.org/10.1093/jge/gxab037.

Zhang, Z. M., Wei, X. D., Yang, H. T., Hu, S. B., Wang, Z. W., and Shi, Y. Z., 2018. Characteristics of Olkaria Geothermal Field, a rift volcanic geothermal system. Sino-Global Energy (in Chinese). 23, no. 12, 16–21. doi: 10.6038/cjg2021N0458.

Zhao, G. K., Hu, Y. Q., Jin, P. H., Hu, Y. F., Li, C., and Zhu, X. Z., 2019. Experimental study on mechanical properties of granite subjected to cyclic loads under real time temperature. Chinese Journal of Rock Mechanics and Engineering. 38, no. 12, 927–937, doi: 10.13722/j.cnki.jrme.2018.1277.